Chinese Chemical Letters 36 (2025) 109586

Contents lists available at ScienceDirect

Chinese Chemical Letters

journal homepage: www.elsevier.com/locate/cclet

AlO_2: A novel two-dimensional material with a high negative Poisson's ratio for the adsorption of volatile organic compounds

Xinghong Cai[a], Qiang Yang[a], Yao Tong[a], Lanyin Liu[a], Wutang Zhang[b,*], Sam Zhang[c,d,*], Min Wang[a,*]

[a] Chongqing Key Laboratory for Advanced Materials and Technologies of Clean Energies, School of Materials and Energy, Southwest University, Chongqing 400715, China
[b] BatteroTech Co., Ltd., Shanghai 201417, China
[c] School of Astronautics, Harbin Institute of Technology, Harbin 150001, China
[d] Zhengzhou Research Institute, Harbin Institute of Technology, Zhengzhou 450000, China

ARTICLE INFO

Article history:
Received 31 December 2023
Revised 25 January 2024
Accepted 29 January 2024
Available online 5 February 2024

Keywords:
AlO_2
Negative Poisson's ratio
VOCs
Two-dimensional material
First-principles calculations

ABSTRACT

We propose and investigate a novel stable two-dimensional (2D) AlO_2 with anomalous stoichiometric ratios based on first-principles calculation. 2D AlO_2 has metallic properties. It possesses the rare in-plane and out-of-plane negative Poisson's ratio (NPR) phenomenon, originating from its special sawtooth-like structure. The absolute value of the NPR decreases as the number of layers increases. The adsorption of volatile organic compounds (VOCs) including CH_2O, C_2H_3Cl and C_6H_6 by AlO_2 exhibit small adsorption distance, large adsorption energy, large charge transfer and significant density of states (DOS) changes, indicating the presence of strong interactions. The desorption time of each gas molecule on the AlO_2 surface is also evaluated, and the results further suggest that the desorption of VOCs can be controlled by changing the temperature to achieve the recycling of AlO_2. These interesting properties make 2D AlO_2 a promising material for electronic, mechanical and sensing applications for VOCs.

Volatile organic compounds (VOCs) are known as dominate precursors to urban haze and photochemical smog, mainly from processes such as coal chemical, petrochemical and fuel paint manufacturing and use [1,2]. Most VOCs are toxic, irritating, teratogenic, and carcinogenic, especially formaldehyde, vinyl chloride, and benzene, which seriously threaten the ecological environment and human health [3–5]. Studies have shown that regular exposure to formaldehyde increases the chance of developing cancers, such as blood and lymphoma [6]. Vinyl chloride enters the body and suppresses the central nervous system, damages the liver and spleen, and produces diseases such as hepatic angiosarcoma [7]. The intake of benzene paralyzes the central nervous system and affects the body's hematopoietic function, leading to aplastic anemia and leukemia in severe cases [8]. Therefore, it is urgent to eliminate VOC pollution. Adsorption technology has gained numerous attentions as an economical and environmentally friendly method in VOC reduction [1].

Because of the interesting physical and chemical performance of 2D metal oxides, they have recently been widely explored in transistors, inverters, photodetectors, memristors, sensors, *etc.* [9,10]. The developments of advanced synthesis methods such as mechanical exfoliation, vapor deposition, and solid solution methods have provided new technical supports for preparing novel layered 2D metal oxides [11,12]. Huang *et al.* [13] proposed that ultrathin 2D Al_2O_3 nanosheets designed by replicating graphene oxide from the bottom up exhibited excellent adsorption capacity for fluoride ions. In addition, HfO_2 [14], In_2O_3 [15], ZnO [16], SnO_2 [17], γ-Bi_2O_3 [18], *etc.*, are also attracting attention as new 2D metal oxides.

Al_2O_3 is widely used in ultrafiltration membranes, catalysts, adsorbents, *etc.*, due to its good electronic properties, mechanical properties and low cost [19–22]. Eunmi *et al.* [23] successfully synthesized porous Al_2O_3 with controlled mesoporous and macroporous characteristics using the solvent defect method to achieve efficient removal of the organic pollutant Congo red dye from water. Kumari *et al.* [24] used nitric-acid-activated Al_2O_3 to increase the efficiency of defluoridation in the industrial wastewater from 74.18% to 97.43%, and the adsorbent exhibited better regeneration and recyclability, which is beneficial for practical industrial applications. Recently, Liu *et al.* [25] found that CO_2 can be effectively

* Corresponding authors.
E-mail addresses: wutang_zhang@163.com (W. Zhang), samzhang@hit.edu.cn (S. Zhang), minwang@swu.edu.cn (M. Wang).

https://doi.org/10.1016/j.cclet.2024.109586
1001-8417/

adsorbed and decomposed on the anoxic γ-Al_2O_3 (100) surface based on first-principles studies. Bai *et al.* [26] found good adsorption of both CS_2 and COF_2 on the surface of α-Al_2O_3 (0001) based on DFT studies. γ-Al_2O_3 showed good adsorption capacity for potentially carcinogenic chlorinated volatile organic compounds (Cl-VOC) such as benzyl chloride, chloroform, and tetrachlorine after 8 weeks of adsorption [27]. We assume and expect that the new AlO_2 in this work can possess some potentials and possibilities for the adsorption of VOCs.

Besides, studying other 2D aluminides has also gained plenty of interests. Wang *et al.* [28] reported 2D AlN synthesized by metal-organic chemical vapor deposition between Si substrate and graphene with ultra-wide bandgap semiconductor (9.63–9.20 eV) showing great promise in deep-UV optoelectronic applications. The 2D Al_2C is a medium bandgap semiconductor (1.02 eV) that maintains its structural integrity at 1500 K, indicating good thermal stability [29] and it was reported to have large adsorption energy (-1.972 eV $\sim$ -2.244 eV) for four toxic VOCs (acetaldehyde, ethylene oxide, vinyl chloride and benzene) and can be used as an adsorbent and sensing medium for toxic VOCs [30]. Wang *et al.* [31] theoretically predicted that the novel monolayer AlP_5 is promising for detecting toxic heavy metals (As, Hg and Cd) in the aqueous environment.

Recently, 2D CaCl and Na_2Cl crystals with abnormal anion and cation ratios generated on graphene films have abnormal physical properties such as metallicity, ferromagnetism and piezoelectric behavior [32,33]. Therefore, the discovery of 2D AlO_2 with abnormal stoichiometry compared with Al_2O_3 is expected to expand the development and application of novel electronic devices. Additionally, AlO_2 molecule and thin film with anomalous stoichiometric ratios have been found experimentally. A new AlO_2 thin film is formed at the interface of diffusion bonding between Pt and α-Al_2O_3 at 1200 °C in Ar atmosphere [34]. Lester *et al.* [35] reacted Al atoms evaporated by pulsed laser with O_2 from a condensing Ar stream to obtain cyclic AlO_2 molecule. The successful syntheses of AlO_2 molecule and thin film promote more explorations of other new kinds of AlO_2 including 2D materials.

Herein, a novel 2D AlO_2 with anomalous stoichiometric ratios is designed based on DFT simulations, and its stability is determined by phonon band structure, calculation of elastic constants and *ab initio* molecular dynamics (AIMD) simulations. The mechanical and electronic performance of monolayer and multilayer AlO_2 are investigated. Interestingly, AlO_2 has a rare in-plane and out-of-plane NPR. In addition, the adsorption performance of AlO_2 on three VOCs (CH_2O, C_2H_3Cl and C_6H_6) is explored. The results show that monolayer AlO_2 has good adsorption and desorption behaviors and is expected to be a potential gas sensor and a good adsorber for detecting and adsorbing VOCs.

The geometry optimization of pristine AlO_2, the calculation of electronic properties and the simulation of adsorbed VOCs on AlO_2 are implemented in the SIESTA code [36] based on DFT [37]. The exchange-correlation term of the generalized gradient approximation (GGA) [38] is performed under the Perdew-Burke-Ernzerhof (PBE) [39] scheme. In order to be closer to the theoretical limit, the double zeta polarization (DZP) [40] function is chosen for the basis set. A $9 \times 12 \times 1$ sampling is used for Monkhorst-Pack grid point sampling, and the set plane wave cut-off energy is 300 Ry. All atoms during the geometry optimizations are completely relaxed until the maximum force is less than 0.02 eV/Å. Furthermore, the thermal and dynamic stability of AlO_2 are confirmed by *ab initio* molecular dynamics (AIMD) [41] simulations based on the canonical ensemble (NVT) and phonon spectrum calculation, respectively. Herein, the canonical ensemble (NVT) refers to the simulated system in which the number of particles (N), volume (V), and temperature (T) remain constant.

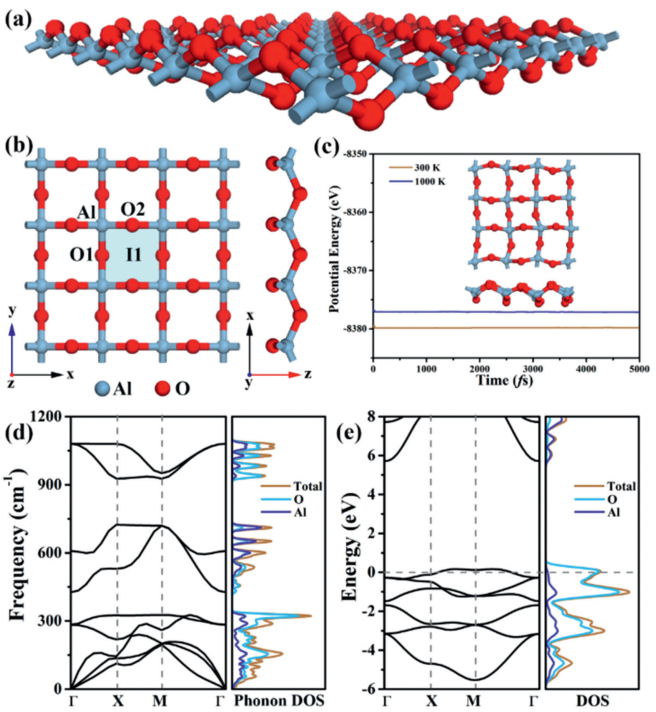

Fig. 1. (a) Geometrically optimized configuration of 2D AlO_2, (b) top and lateral views. The unit cell is marked with a light blue rectangular area. Four possible adsorption sites (O1, O2, Al1 and I1) are marked. (c) Potential energy fluctuations of AlO_2 in AIMD simulations at 300 and 1000 K, and the inset shows the structure after 5 ps of AIMD simulations at 1000 K. (d) Phonon band structure and phonon DOS of AlO_2. (e) Band structure of AlO_2 and the corresponding DOS.

To determine the stability of multilayer AlO_2, we define the formation energy (E_f) as:

$$E_f = E(\text{n-AlO}_2) - \text{n}E(\text{AlO}_2) \quad (1)$$

where n is the number of layers of AlO_2; $E(AlO_2)$ and E(n-AlO_2) denote the total energy of single-layer and n-layer AlO_2, respectively.

In order to accurately describe the adsorption properties of VOCs on the AlO_2 surface, we define the adsorption energy (E_{ads}) as:

$$E_{ads} = E(\text{AlO}_2\text{-VOCs}) - E(\text{AlO}_2) - E(\text{VOCs}) \quad (2)$$

where $E(AlO_2)$ and E(VOCs) are the energy of the original AlO_2 and independent VOCs gas molecules, respectively, and E(AlO_2-VOCs) is the total energy of the adsorption system of VOCs molecules.

The differential charge density between AlO_2 and VOCs molecules in the adsorption system is defined as:

$$\Delta\rho = \rho(\text{AlO}_2\text{-VOCs}) - \rho(\text{AlO}_2) - \rho(\text{VOCs}) \quad (3)$$

where $\rho(AlO_2)$ and ρ(VOCs) denote the charge values of original AlO_2 and independent VOCs gas molecules, respectively, and ρ(AlO_2-VOCs) denotes the total charge value of the adsorption system of VOCs molecules.

The optimized 2D AlO_2 structure is shown in Figs. 1a and b, which has a *P-4m2* space group and belongs to the tetragonal crystal system ($a = b = 3.27$ Å, $c = 15$ Å, $\alpha = \beta = \gamma = 90°$), and each cell includes one Al atom and two O atoms (see the light blue area in Fig. 1b). Section S7 (Supporting information) lists the specific position of each atom in the unit cell. The 2D AlO_2 is a sawtooth-like structure with a monolayer height of $d = 1.45$ Å, as shown in the side view of Fig. 1b. The outer and inner atoms are O and

Al ones, respectively. The Al-O bond has a bond length of 1.79 Å, which is close to the theoretical data of the Al-O bond length of α-Al_2O_3 (1.68–1.86 Å) [42] and γ-Al_2O_3 (1.75–1.77 Å) [43]. The bond angle of Al-O-Al is 132.14°. Additionally, AlO_2 has anomalous stoichiometric ratios. The oxidation states may be abnormal. Lu *et al.* [34] reported that the possible form of AlO_2 is $(Al^{3+})_2(O_2)^{2-}(O^{2-})_2$. Possible oxidation states of AlO_2 may be Al^{3+}, O^{2-} and O^-.

The stability of AlO_2 is evaluated by molecular dynamics (MD) simulations, phonon spectra and strain energy calculations. The results of MD simulation for AlO_2 are plotted in Fig. 1c. It is obvious that no significant deformation and bond breaking occur in the structure of AlO_2 heated at 300 K and 1000 K for 5 ps, and its potential energies at 300 K and 1000 K have few changes, indicating that AlO_2 still has good thermal stability at 1000 K. The phonon spectrum of AlO_2 is shown in Fig. 1d, and no imaginary frequencies are observed throughout the Brillouin zone, confirming the dynamic stability of AlO_2. The maximum vibrational frequency of 1080.5 cm^{-1} is contributed by both Al and O atoms, which facilitates future experimental characterization. To further determine the mechanical stability of AlO_2, the calculated elastic constants of $C_{11} = 48.23$ N/m, $C_{12} = -12.32$ N/m, $C_{22} = 48.23$ N/m and $C_{44} = 1.25$ N/m fully satisfy the Born-Huang criterion: $C_{44} > 0$ and $C_{11}C_{22}\text{-}C_{12}^2 > 0$, indicating that AlO_2 is mechanically stable.

In addition, the conductivity of AlO_2 material is verified by calculating electronic properties. The valence band top of the band structure crosses the Fermi energy level (Fig. 1e), indicating that AlO_2 is metallic. The contribution of O atoms near the Fermi level leads to a non-zero density of states (DOS), further proving the metallicity of AlO_2. The electronic properties of AlO_2 are similar to those of graphene oxide, which has a negative differential resistance (NDR) phenomenon [44], suggesting that AlO_2 is promising for NDR nanodevices.

The flexibility or rigidity of the material is defined by the in-plane stiffness C, and flexible materials have less in-plane stiffness. The strain energy curves of AlO_2 are shown in Fig. 2a. As shown in Fig. 2b, the in-plane stiffness along the x or y orientation is 48.23 N/m, which is considerably smaller than that of graphene (341 N/m) [45] and MoS_2 (120.1 N/m) [46], but a little larger than those of g-C_3N_5 (37 N/m) [47] and g-ZnO (47.8 N/m) [48]. It is noted that when θ equals 45°, 135°, 225° and 315°, the corresponding in-plane stiffness is only 1.08 N/m. Such small in-plane stiffness along the diagonal direction indicates more flexibility and more softness than those along the x and y axes, which is attributed to its pleated structure. Poisson's ratio ν is defined as the ratio of lateral versus vertical strain of the material, and reflects the elastic constant of the lateral distortion of the material. As illustrated in Fig. 2c, AlO_2 has a large ν of 0.97 along the diagonal direction. However, a rare negative Poisson's ratio (NPR) of −0.26 appears in the x and y orientations. Such NPR phenomenon mainly originates from its characteristic sawtooth configuration in the x and y directions, similar phenomena have been reported in structures such as black phosphorus [49], BP_5 [50] and penta-graphene [51]. To further compare the NPR properties of AlO_2, the Poisson's ratios of different two-dimensional materials with NPR properties predicted by recent theories are listed in Fig. 2d. The results show that the NPR performance of AlO_2 materials is superior compared to the majority of 2D materials such as borophane (−0.053) [52], penta-graphene (−0.068) [51], phosphorene (−0.027) [53], SiS (−0.19) [54], Ag_2S (−0.12) [55] and SnSe (−0.17) [56]. Due to the special mechanical properties of NPR materials, they have broad application prospects in aerospace, medical equipment, sensors, protective equipment and other fields [57].

In order to explore the origination of the in-plane NPR of the single-layer AlO_2 structure, we investigate the changes of the angle ∠OAlO under x-axis strain. As shown in Fig. S1, ∠OAlO increases by 0.88% and decreases by 1.27% under tensile and compressive strains, respectively. Therefore, the in-plane NPR of AlO_2 mainly comes from the contribution of the angle ∠OAlO, as schematically shown in Figs. 2e and f.

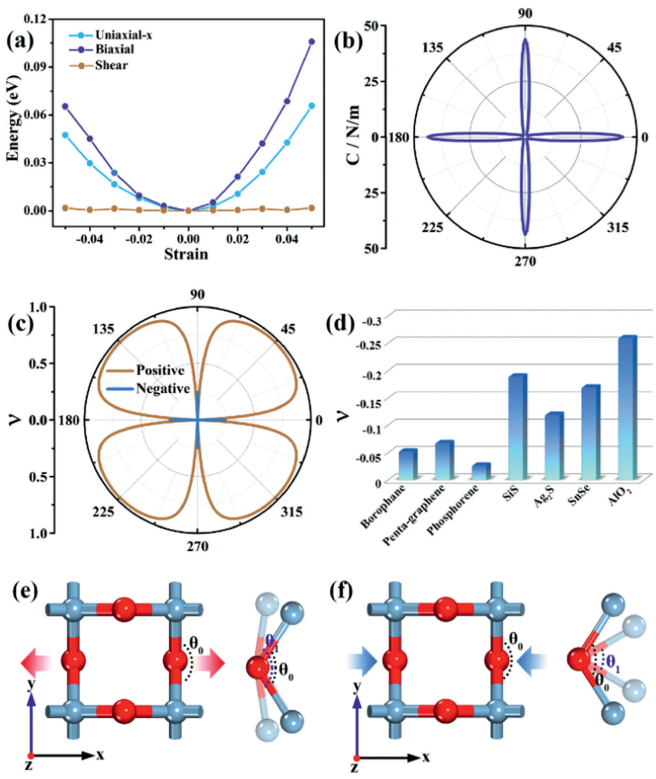

Fig. 2. (a) AlO_2 strain energy under various strains. (b) In-plane stiffness C and (c) Poisson's ratio ν of AlO_2. (d) Comparison of in-plane Poisson's ratios of some 2D materials. The schematic images of in-plane NPR phenomenon caused by the angle ∠OAlO of AlO_2 under transverse (e) stretching and (f) compression.

Since it is much easier to experimentally synthesize multilayer structures, the formation energy, DOS, C, ν and electronic properties of 1–5 layers of AlO_2 are considered. The structures of 1–5 layers of AlO_2 after geometry optimizations are shown in Fig. 3a, and the total layer thickness from 1.45 Å to 17.46 Å as the number of layers increases. In order to study the stability of multilayer AlO_2, the calculation of formation energy is performed according to Eq. 1. Fig. 3b shows the variation of formation energy of 2–5 layers of AlO_2 nanosheets, with the increase of the number of layers, the formation energy is more negative, which indicates the increased stability of the multilayer structure.

The total DOS of 1–5 layers of AlO_2 is shown in Fig. 3c. The DOS of all multilayer AlO_2 crosses the Fermi level, confirming their conducting behavior, which is consistent with the band structures (Fig. S3 in Supporting information). As the number of layers increases, the DOS also increases, which is consistent with the increase in the number of energy bands. In addition, the DOS maps of 1–5 layers of AlO_2 are similar, with all DOS peaks locate at nearly the same energy, suggesting that the multilayer AlO_2 structures relies mainly on van der Waals interactions between neighboring layers.

The C and ν as a function of angle for 1–5 layers of AlO_2 are shown in Figs. 3d and e. The in-plane stiffness and positive Poisson's ratio decrease as the layers increase. The NPR performance of the monolayer structure is still maintained for multilayer AlO_2, however the NPR values along the x and y axes increase from −0.26 to −0.08 as the number of layers increases (Table S1 in Supporting information). Therefore, the tuning of mechanical properties such as in-plane stiffness and Poisson's ratio of AlO_2 can be achieved by different numbers of layers.

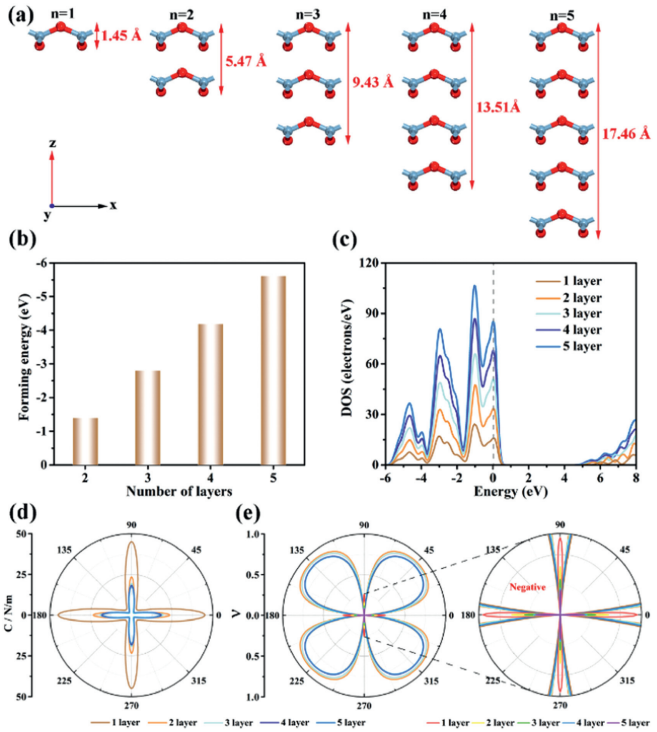

Fig. 3. (a) Side view of the geometry of 1–5 layers AlO_2 with the intra-layer heights marked. (b) Forming energy of 2–5 layers of AlO_2. (c) The DOS of 1–5 layers AlO_2. (d) In-plane stiffness C and (e) Poisson's ratio ν of 1–5 layers AlO_2. The inset shows an enlarged view of the NPR in (e).

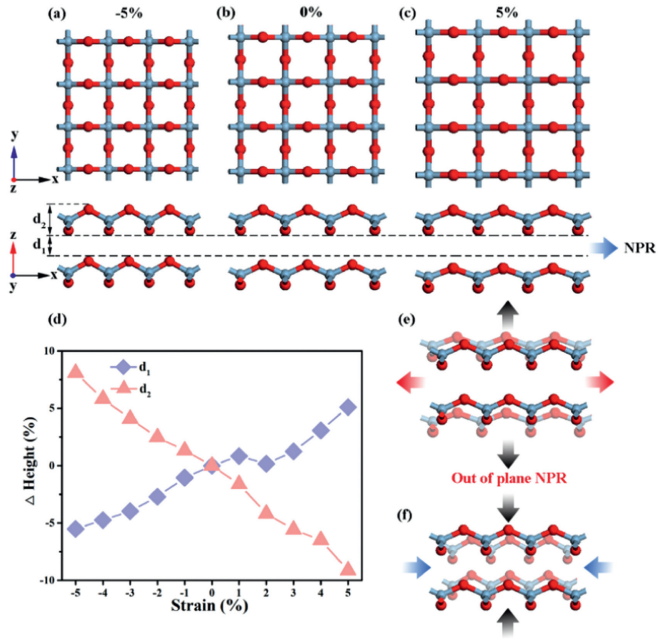

Fig. 4. Top and side views of the bilayer AlO_2 structure under biaxial strain of (a) −5%, (b) 0%, and (c) 5%. d_1 denotes the interlayer height of bilayer AlO_2. d_2 denotes the intra-layer height of single-layer AlO_2. (d) Percentage change of interlayer height d_1 and intra-layer height d_2 with biaxial strain. (e) Longitudinal expansion phenomenon of bilayer AlO_2 in the case of transverse stretching. (f) Longitudinal shrinkage phenomenon of bilayer AlO_2 under lateral compression.

To explore the out-of-plane NPR of the bilayer structure, we compare the variation of interlayer height d_1 and intra-layer height d_2 in the bilayer AlO_2 structure under different biaxial strains. The typical structures of the bilayer AlO_2 after geometric optimization under the biaxial strains of −5%, 0% and 5% are shown in Figs. 4a–c. Obviously, with the applied compressive and tensile strains, the interlayer height d_1 decreases and increases in the side view of Figs. 4a–c, respectively, revealing that the bilayer AlO_2 has an out-of-plane NPR. Furthermore, the comprehensive variations of d_1 and d_2 with different biaxial strains are demonstrated in Fig. 4d. The results exhibit that by applying −5% compressive (or 5% tensile) strain in the transverse direction, d_1 decreases by 5.5% (or increases by 5.1%); on the other hand, d_2 increases by 8.1% (or reduces by 9.1%). Thus the out-of-plane NPR of bilayer AlO_2 comes mainly from the contribution of the interlayer height d_1. The schematic diagram of the out-of-plane NPR of bilayer AlO_2 is shown in Figs. 4e and f. AlO_2 becomes thicker or thinner vertically when it experiences transverse tensile or compressive strain respectively (Figs. 4e and f), similar to other 2D materials such as black phosphorene [58] and borophane [52] possessing out-of-plane NPR.

The adsorption performance is investigated to explore the potential application of AlO_2 in VOC detection. As shown in Fig. 1b, there are three types of adsorption sites in the AlO_2 structure: atomic tops (A1, O1, and O2), the middle of the bonds (Al-O1 and Al-O2), and hollow (I1). VOC molecules are placed in the positions mentioned above to find a suitable adsorption conformation, and then the geometry is optimized without imposing any constraints. The most negative adsorption energy is used as a criterion to find the most stable adsorption conformation. Figs. 5a–c show the most stable adsorption configurations of three VOCs adsorbed on AlO_2. The adsorption energies of the AlO_2-CH_2O, AlO_2-C_2H_3Cl and AlO_2-C_6H_6 parallel (and vertical) adsorption systems are −0.84 eV (−0.51 eV), −1.19 eV (−0.72 eV) and −1.18 eV (−0.29 eV), respectively. The adsorption energies of the parallel systems are more negative than those of the vertical systems. CH_2O, C_2H_3Cl and C_6H_6 are parallel to the AlO_2 plane with adsorption distances of 1.97 Å, 1.90 Å and 2.19 Å, respectively. Mulliken charge analysis is performed for the most stable adsorption configurations, as shown in Figs. 5d–f, revealing that all VOC molecules act as charge donors and AlO_2 acts as charge acceptors. The charge transfer amount of the adsorption system is defined as: $\Delta Q = Q(^*\text{VOCs}) - Q(\text{VOCs})$, where $Q(^*\text{VOCs})$ denotes the charge of VOCs gas in the adsorption system, and $Q(\text{VOCs})$ denotes the charge values of independent VOCs gas molecules. The charge loss of CH_2O, C_2H_3Cl and C_6H_6 molecules are −0.36 e, −0.64 e and −0.77 e, respectively.

To further compare the adsorption stability of AlO_2, the adsorption energies and charge transfer amounts of VOCs on the surfaces of different 2D materials (MoBOH [59], phospholene [60], MnO_2 [61], Pd-C_3N [62], Ni-HfSSe [63], Al_2C [30] and F-diamane [64]) are presented in Fig. 5j. As a comparison, the adsorption energies of VOCs for the structures provided in previous works (MnO_2 [61] and phospholene [60]) are calculated. The adsorption energies of MnO_2-CH_2O, MnO_2-C_6H_6 and phospholene-CH_2O are −0.52 eV, −0.24 eV and −0.56 eV, respectively. These data are close to those reported works [60,61]. The results show that the two-dimensional AlO_2 material exhibits a better adsorption effect on VOCs and the adsorption energy is better than most 2D materials. The AlO_2 surface has satisfactory VOCS desorption compared to Pd-C_3N and Al_2C, which have higher adsorption energy. It must be noted that too high adsorption energy is not conducive to VOCs desorption and material recovery. The charge transfer is much larger than that of several other 2D materials, confirming the strong interaction of VOCs with AlO_2. The low adsorption distance, high adsorption energy and large charge transfer demonstrate the high efficiency of 2D AlO_2 for removing these VOCs.

As shown in Figs. 5g–i, DOS analysis is also performed to examine the effect of the adsorption of VOCs on the electronic characteristics of AlO_2. The total DOS before and after the adsorption

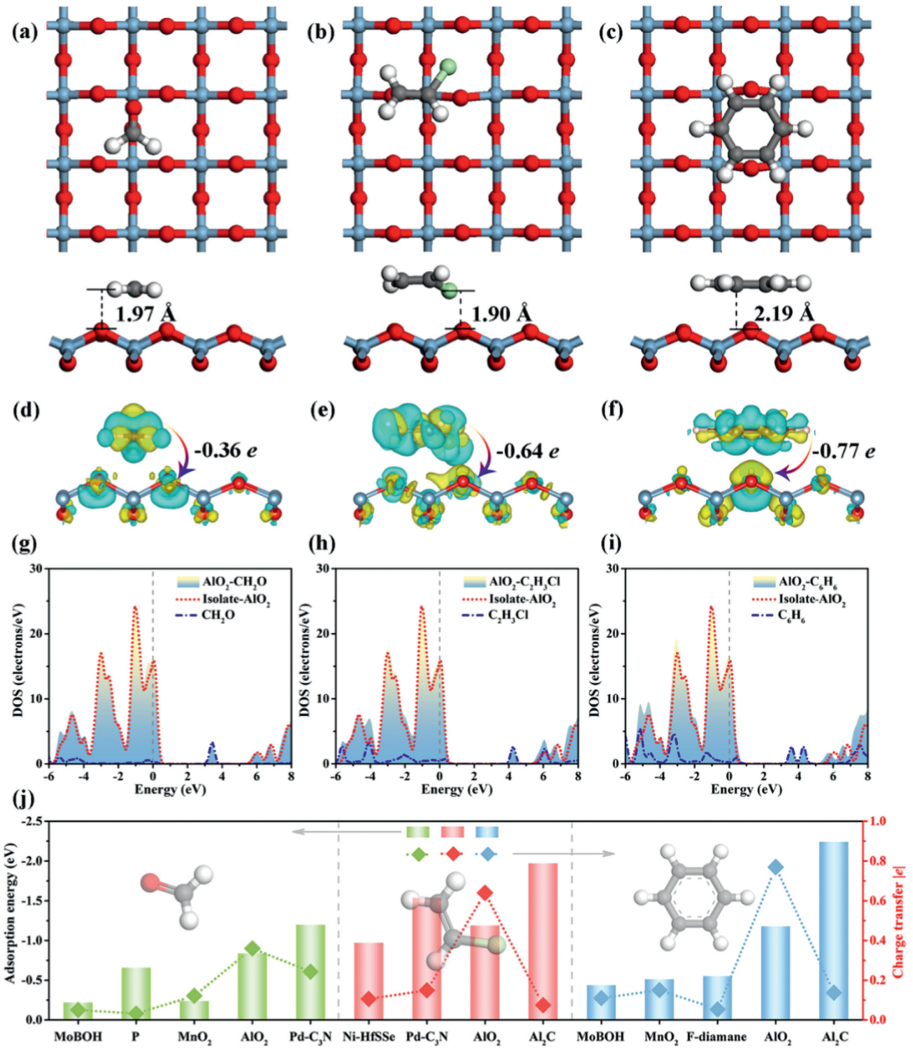

Fig. 5. Stable configurations and charge density differences of (a, d) CH_2O, (b, e) C_2H_3Cl and (c, f) C_6H_6 adsorbed on the surface of AlO_2. The red, blue, gray, white and green balls are used to denote O, Al, C, H and Cl atoms. The value of 0.025 e/Å^3 is determined as the isosurface. The amount and direction of charge transferred in the adsorption system are marked. The DOS before and after adsorption of (g) CH_2O, (h) C_2H_3Cl and (i) C_6H_6 by monolayer AlO_2. (j) Comparison of adsorption energies and charge transfers of some 2D materials for the adsorption of VOCs.

of VOCs appear to be significantly different. After adsorption of VOCs molecules on AlO_2, VOCs molecules not only have a significant contribution to the valence band but also have a major contribution to the conduction band, which is consistent with the band structures (Fig. S4 in Supporting information). Significant changes in the DOS before and after adsorption of VOCs molecules indicate the presence of strong interactions between AlO_2 and VOCs, which is consistent with the results of large charge transfer amounts.

The effectiveness of VOCs desorption is mainly determined by the recovery time, which is the time the sensor needed to return to its original state after the gas is removed. Therefore, according to the transition state principle, the recovery time (τ) of VOCs molecules on the AlO_2 surface is evaluated:

$$\tau = A^{-1} e^{\left(-E_{ads}/k_B T\right)} \quad (4)$$

where A (10^{12} s^{-1}) is the apparent frequency factor, k_B (8.62×10^{-5} eV/K) is the Boltzmann constant, E_{ads} (eV) is the adsorption energy which is the energy barrier of the desorption process, and T (K) is the system temperature. As shown in Fig. 6, the desorption times of VOCs molecules on the AlO_2 surface at different temperatures are calculated. CH_2O has a short recovery time (1.69×10^2 s) at room temperature, indicating that the

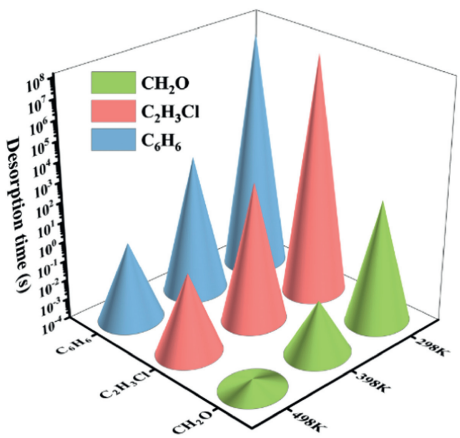

Fig. 6. Desorption time of CH_2O, C_2H_3Cl and C_6H_6 molecules on AlO_2 surface at different temperatures.

AlO_2 sensor is expected to detect CH_2O at room temperature reversibly. The long desorption time of C_2H_3Cl (1.36×10^8 s) and C_6H_6 (9.93×10^7 s) implies that AlO_2 is suitable as an adsorbent

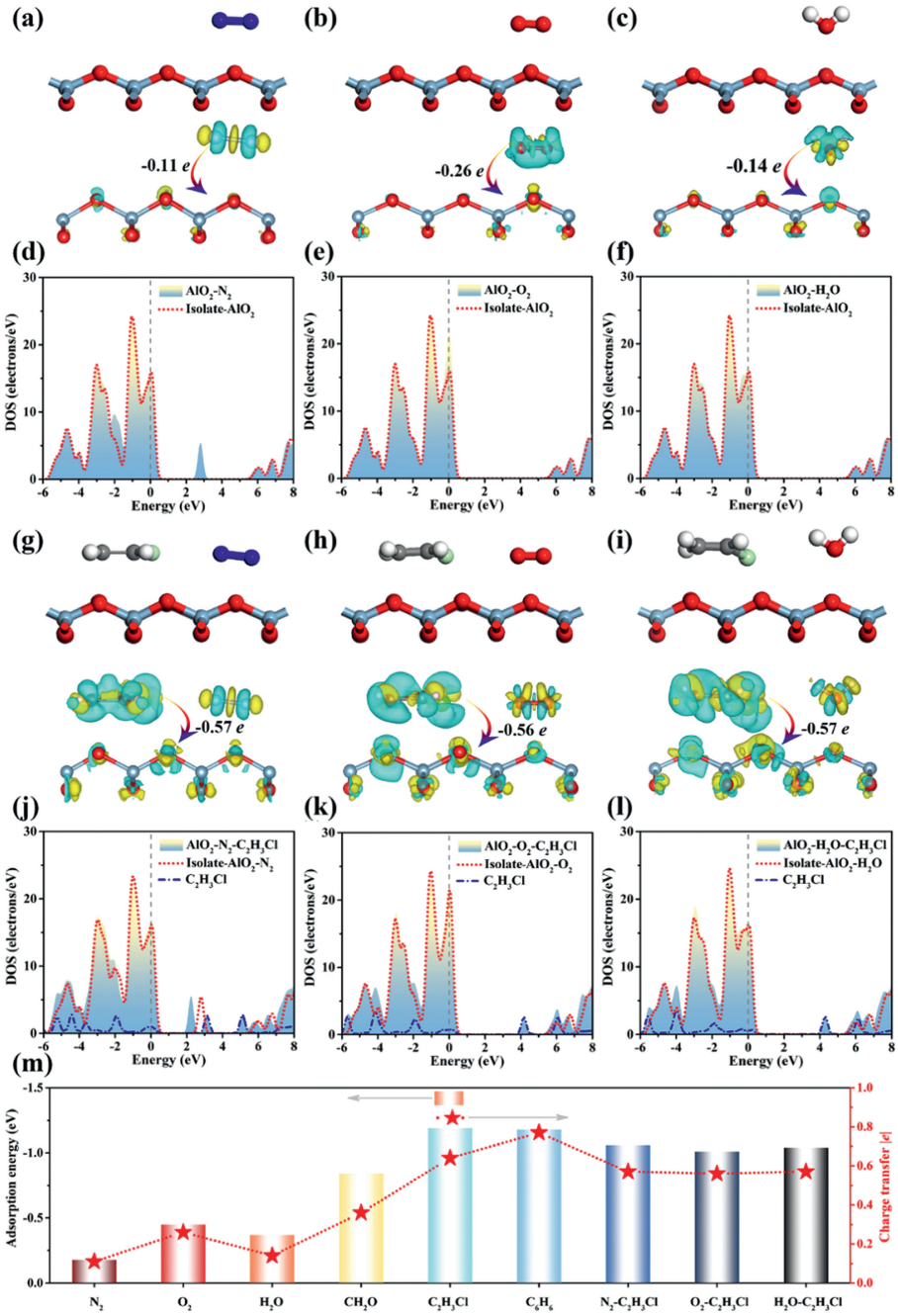

Fig. 7. Stable configurations, charge density differences and DOS of (a, d) N_2, (b, e) O_2, (c, f) H_2O, (g, j) N_2-C_2H_3Cl, (h, k) O_2-C_2H_3Cl and (i, l) H_2O-C_2H_3Cl adsorbed on the surface of AlO_2. (m) Comparison of adsorption energies and charge transfers of monolayer AlO_2 for the adsorption of gas molecular and C_2H_3Cl (in O_2, N_2 and water environment).

for C_2H_3Cl and C_6H_6 at room temperature. In addition, the desorption time decreases with increasing temperature. For C_2H_3Cl and C_6H_6 molecules, the desorption times at 498 K are 1.11 s and 0.92 s, respectively, indicating that the high temperature accelerates desorption. Therefore, at room temperature, AlO_2 can be used as a gas sensor for the detection of CH_2O and an adsorbent for C_2H_3Cl and C_6H_6; and at higher temperatures, it can also act as a gas sensor for the detection of C_2H_3Cl and C_6H_6.

For the future applications, the O_2, N_2 and water effects should be considered. Since AlO_2 has the maximum adsorption energy for C_2H_3Cl, we continue to consider the effect of O_2, N_2 and H_2O molecules on the adsorption of C_2H_3Cl. As shown in Figs. 7a–f, the adsorption energies (−0.18 eV, −0.45 eV and −0.37 eV) and the amounts of the charge transfer (−0.11 e, −0.26 e and −0.14 e) of N_2, O_2 and H_2O on the AlO_2 surface are much smaller than those of C_2H_3Cl on AlO_2. Figs. 7g–l display the geometry, charge difference density distribution and DOS of C_2H_3Cl adsorbed on the AlO_2 surface in O_2, N_2 and water environment, respectively. As shown in Fig. 7m, the adsorption energies (−1.06 eV, −1.01 eV and −1.04 eV) and the amounts of charge transfer (−0.56 e, −0.57 e and −0.57 e) of C_2H_3Cl on AlO_2 in O_2, N_2 and water environment are slightly lower than those in the vacuum environment. Therefore, the effect of the presence of O_2, N_2 and H_2O on the adsorption of C_2H_3Cl on the AlO_2 surface is insignificant.

In summary, we propose a novel 2D AlO_2 with anomalous stoichiometric ratios. The phonon spectra, AIMD simulations and elas-

tic constants confirm its stability. Electronic calculations show that AlO_2 is a conductor. Due to its special structure of serrated configuration, AlO_2 offers low in-plane stiffness and a large negative Poisson's ratio (NPR). The Poisson's ratio of 1–5 layers of AlO_2 is negative, and the absolute value of NPR decreases as the number of layers increases. The bilayer AlO_2 exhibits a rare NPR in both in-plane and out-of-plane directions and reveals the underlying mechanism. The potential applications of AlO_2 in the adsorption of CH_2O, C_2H_3Cl and C_6H_6 detection are explored. The low adsorption distance (1.90 Å to 2.19 Å), high adsorption energy (−0.84 eV to −1.19 eV) and large charge transfer (−0.36 e to −0.77 e) indicate the high removal efficiency of 2D AlO_2 for these VOCs. The DOS of AlO_2 changed significantly before and after the adsorption of VOC molecules, indicating the presence of strong interactions between AlO_2 and VOCs. The evaluation of the desorption time revealed that AlO_2 could be used as an adsorbent or gas sensors for VOCs at room or higher temperatures. Besides adsorption of VOCs on the bare AlO_2 situations, we also investigate the adsorption of C_2H_3Cl on the AlO_2 surface in N_2, O_2, and water environment to support the possible applications of AlO_2. Compared with normal Al_2O_3, 2D AlO_2 with abnormal stoichiometric ratios can not only extend aluminum-oxide materials, but also provide some interesting properties including a high NPR and good adsorption of VOCs. Moreover, 2D AlO_2 has potentials for the novel mechanical and electronic devices. Therefore, this research is expected to provide new insights into the development and application of AlO_2 and other 2D materials.

Declaration of competing interest

The authors declare that they have no known competing financial interests or personal relationships that could have appeared to influence the work reported in this paper.

Acknowledgments

This work was financially supported by National Natural Science Foundation of China (No. 22275149), Fundamental Research Funds for the Central Universities (No. SWU118105) and the Next-Generation Advanced Energy Materials Program of BatteroTech Co., Ltd.

Supplementary materials

Supplementary material associated with this article can be found, in the online version, at doi:10.1016/j.cclet.2024.109586.

References

[1] X. Li, L. Zhang, Z. Yang, et al., Sep. Purif. Technol. 235 (2020) 116213.
[2] X. Ma, L. Yang, H. Wu, J. Clean. Prod. 302 (2021) 126925.
[3] H. Dai, S. Jing, H. Wang, et al., Sci. Total Environ. 577 (2017) 73–83.
[4] B. Liu, W. Zhao, Q. Jiang, et al., Sustain. Mater. Technol. 21 (2019) e00103.
[5] K. Vikrant, H. Yang, M.W. Chung, et al., Mater. Today Nano 21 (2023) 100283.
[6] M. Hauptmann, J.H. Lubin, P.A. Stewart, et al., J. Natl. Cancer Inst. 95 (2003) 1615–1623.
[7] J. Kielhorn, C. Melber, U. Wahnschaffe, et al., Environ. Health Perspect. 108 (2000) 579–588.
[8] V. Bollati, A. Baccarelli, L. Hou, et al., Cancer Res. 67 (2007) 876–880.
[9] Z. Hu, X. Xiao, H. Jin, et al., Nat. Commun. 8 (2017) 15630.
[10] P. Kumbhakar, C.C. Gowda, P.L. Mahapatra, et al., Mater. Today 45 (2021) 142–168.
[11] J. Mei, T. Liao, L. Kou, et al., Adv. Mater. 29 (2017) 1700176.
[12] H. Zhao, Y. Zhu, F. Li, et al., Angew. Chem. Int. Ed. 56 (2017) 8766–8770.
[13] Z. Huang, A. Zhou, J. Wu, et al., Adv. Mater. 28 (2016) 1703–1708.
[14] A. Zavabeti, J.Z. Ou, B.J. Carey, et al., Science 358 (2017) 332–335.
[15] A. Jannat, N. Syed, K. Xu, et al., ACS Nano 15 (2021) 4045–4053.
[16] N. Mahmood, H. Khan, K. Tran, et al., Mater. Today 44 (2021) 69–77.
[17] C.H. Huang, H. Chang, T.Y. Yang, et al., ACS Appl. Mater. Interfaces 13 (2021) 52822–52832.
[18] J. Wu, F. Wang, H. Li, et al., Small 18 (2022) 2104244.
[19] J. Ma, Z. Liu, J. Song, et al., Green Chem. 20 (2018) 5188–5195.
[20] W. Shi, C. Yang, M. Qiu, et al., J. Membr. Sci. 642 (2022) 119992.
[21] W. Fu, Z. Li, W. Xu, et al., Mater. Today Nano 11 (2020) 100088.
[22] H. Wang, Y. Liu, J. Song, et al., Mater. Today Nano 20 (2022) 100244.
[23] E. Im, H.J. Seo, D.I. Kim, et al., Chem. Eng. J. 416 (2021) 129147.
[24] U. Kumari, S.K. Behera, H. Siddiqi, et al., J. Hazard. Mater. 381 (2020) 120917.
[25] S. Liu, Z. Zhou, J. Chen, et al., Appl. Surf. Sci. 611 (2023) 155645.
[26] Y. Bai, G. Wei, Z. Cao, et al., Appl. Surf. Sci. 577 (2022) 151933.
[27] S.A. Halawy, A.I. Osman, N. Mehta, et al., Chemosphere 295 (2022) 133795.
[28] W. Wang, Y. Zheng, X. Li, et al., Adv. Mater. 31 (2019) 1803448.
[29] Y. Li, Y. Liao, P.V.R. Schleyer, et al., Nanoscale 6 (2014) 10784–10791.
[30] R. Rahimi, M. Solimannejad, A. Chaudhari, J. Hazard. Mater. 403 (2021) 123600.
[31] M. Wang, X. Cai, Q. Yang, et al., Appl. Surf. Sci. 623 (2023) 157025.
[32] Y. Yang, B. Peng, X. Lei, et al., Prog. Chem. 34 (2022) 1524–1536.
[33] X. Xia, Y. Huang, B. Peng, et al., Adv. Mater. 35 (2023) 2303072.
[34] Y.C. Lu, R. Dieckmann, S.L. Sass, J. Phys. Chem. Solids 55 (1994) 1083–1095.
[35] L. Andrews, T.R. Burkholder, J.T. Yustein, J. Phys. Chem. 96 (1992) 10182–10189.
[36] J.M. Soler, E. Artacho, J.D. Gale, et al., J. Phys. Condens. Mater. 14 (2002) 2745–2779.
[37] P.J. Stephens, F.J. Devlin, C.F. Chabalowski, et al., J. Phys. Chem. 98 (1994) 11623–11627.
[38] J.P. Perdew, K. Burke, M. Ernzerhof, Phys. Rev. Lett. 77 (1996) 3865–3868.
[39] B. Hammer, L.B. Hansen, J.K. Norskov, Phys. Rev. B 59 (1999) 7413–7421.
[40] A. Canal Neto, F.E. Jorge, Chem. Phys. Lett. 582 (2013) 158–162.
[41] M. Thomas, M. Brehm, R. Fligg, et al., Phys. Chem. Chem. Phys. 15 (2013) 6608–6622.
[42] S.Q. Zhou, X.H. Ju, F.Q. Zhao, et al., Appl. Surf. Sci. 258 (2012) 7334–7342.
[43] R. Kiruba, S. Vinod, A.W. Zaibudeen, et al., Colloids Surf. A 555 (2018) 63–71.
[44] M. Wang, C.M. Li, Phys. Chem. Chem. Phys. 13 (2011) 1413–1418.
[45] Q. Peng, C. Liang, W. Ji, et al., Phys. Chem. Chem. Phys. 15 (2013) 2003–2011.
[46] Q. Peng, S. De, Phys. Chem. Chem. Phys. 15 (2013) 19427–19437.
[47] Q. Yang, X.H. Cai, Y. Pang, et al., Int. J. Quantum Chem. 120 (2020) e26378.
[48] Q. Peng, C. Liang, W. Ji, et al., Comput. Mater. Sci. 68 (2013) 320–324.
[49] J.W. Jiang, H.S. Park, Nat. Commun. 5 (2014) 4727.
[50] H. Wang, X. Li, J. Sun, et al., 2D Mater. 4 (2017) 045020.
[51] S. Zhang, J. Zhou, Q. Wang, et al., Proc. Natl. Acad. Sci. U. S. A. 112 (2015) 2372–2377.
[52] L. Kou, Y. Ma, C. Tang, et al., Nano Lett. 16 (2016) 7910–7914.
[53] H. Wang, X. Li, P. Li, et al., Nanoscale 9 (2017) 850–855.
[54] T. Jing, D. Liang, M. Deng, et al., J. Mater. Chem. C 8 (2020) 10382–10389.
[55] R. Peng, Y. Ma, Z. He, et al., Nano Lett. 19 (2019) 1227–1233.
[56] L.C. Zhang, G. Qin, W.Z. Fang, et al., Sci. Rep. 6 (2016) 19830.
[57] C. Huang, L. Chen, Adv. Mater. 28 (2016) 8079–8096.
[58] Y. Du, J. Maassen, W. Wu, et al., Nano Lett. 16 (2016) 6701–6708.
[59] D. Li, X. Chen, C. Shu, et al., Appl. Surf. Sci. 563 (2021) 150233.
[60] A. Aasi, S.M. Aghaei, B. Panchapakesan, J. Mater. Chem. C 9 (2021) 9242–9250.
[61] J. Cao, F. Wu, M. Wen, et al., Appl. Surf. Sci. 539 (2021) 148164.
[62] L. Gao, P. Feng, Y. Sun, et al., Comput. Theor. Chem. 1209 (2022) 113611.
[63] Q. Zhao, Y. Man, S. Li, et al., Comput. Theor. Chem. 1214 (2022) 113744.
[64] Y. Liu, L. Gao, S. Fu, et al., Appl. Surf. Sci. 611 (2023) 155694.